4

Source Considerations in Radiographic Imaging

In Chapter 3, which emphasized attenuation mechanisms, a parallel x-ray source was assumed. In this chapter we study the limits imposed by an x-ray source of finite size.

POINT-SOURCE GEOMETRY

In radiography the sources approach point sources resulting from an electron beam striking a metal target. The use of a point source, with its associated diverging beam, results in "distorted" projection images compared to those of the parallel beam studied in Chapter 3 [Christensen et al., 1978]. A typical x-ray tube is shown in Fig. 4.1 [Ter-Pogossian, 1967]. The electron beam, accelerated to about 100 kv, is used to bombard a tungsten anode. Since the exposure times are a small fraction of a second, the anode heating is minimized by using a rotating anode and thus providing a larger dissipation surface. The electron

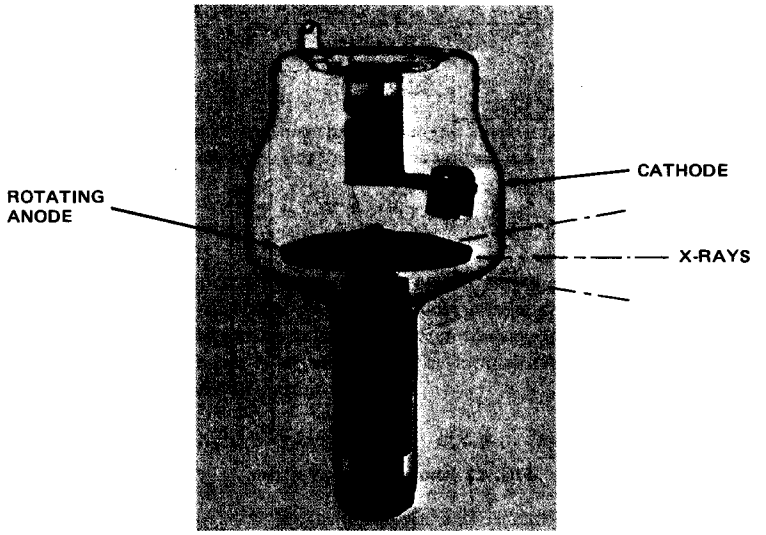

FIG. 4.1 Rotating anode x-ray tube. (Courtesy of the Machlett Laboratories, Inc.)

beam strikes a tilted surface so that the projected focal spot, in the direction of the beam, is smaller than the bombarded area.

We first consider the geometry formed by an ideal point source as shown in Fig. 4.2. The output is formed by the line integral of the attenuation coefficient $\mu(x, y, z)$ of the various rays. In studying the geometric considerations relating to image distortion and resolution, it is convenient to assume a monoenergetic source. This represents no loss of generality since we can always return to the general relationship as expressed in equation (3.4). Thus the detector output due to a monoenergetic source is given by

$$I_d(x_d, y_d) = I_i(x_d, y_d) \exp\left[-\int \mu_0(x, y, z)dr\right] \tag{4.1}$$

where $I_i(x_d, y_d)$ is the intensity incident on the detector plane in the absence of any attenuation and $\mu_0(x, y, z)$ is the linear attenuation coefficient at the monochromatic energy $\mathcal{E}_0$.

This intensity $I_i(x_d, y_d)$ in the absence of any attenuating object can be evaluated with the aid of Fig. 4.3. A point radiator emits N photons isotropically during the exposure interval. The intensity at a point x_d, y_d in the detector plane is proportional to the number of photons per unit area at that point as

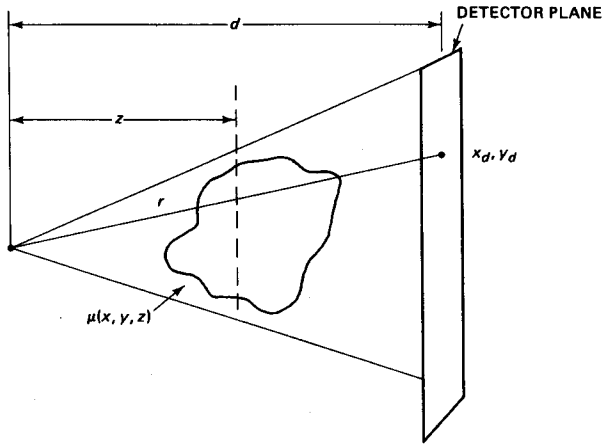

FIG. 4.2 Point-source x-ray system.

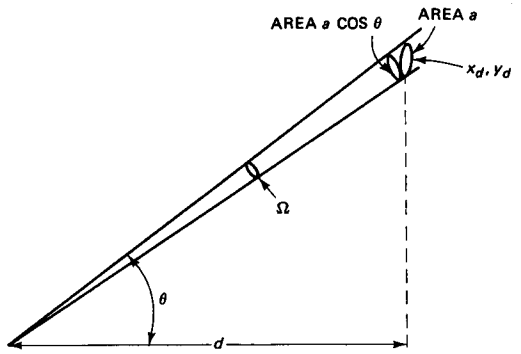

FIG. 4.3 Intensity falloff of an incident beam.

given by

$$I_i(x_d, y_d) = K\frac{N\Omega}{4\pi a} \tag{4.2}$$

where $N\Omega/4\pi$ is the number of photons in Ω, a is the incremental area, K is a constant representing the energy per photon, and Ω is the solid angle intercepted by the area a given by

$$\Omega = \frac{a\cos\theta}{r^2}. \tag{4.3}$$

It is often convenient to specify $I_i(x_d, y_d)$ in terms of I_0, its value at the origin, where $\theta = 0$, as given by

$$I_0 = \frac{KN}{4\pi d^2}. \tag{4.4}$$

This provides a representation that shows the variations in incident intensity with detector coordinates. Thus I_i can be expressed as

$$I_i = I_0\cos^3\theta = I_0\frac{1}{(1 + r_d^2/d^2)^{3/2}} \tag{4.5}$$

where $r_d^2 = x_d^2 + y_d^2$.

This $\cos^3\theta$ dependence can be interpreted as the product of an inverse square falloff with distance, providing a $\cos^2\theta$ dependence, multiplied by a $\cos\theta$ dependence due to the obliquity between the rays and the detector plane. Thus far the source has been assumed to be monoenergetic. For a polychromatic source the detector output becomes

$$I_d(x_d, y_d) = \int I_i(\mathcal{E})\exp\left[-\int \mu(x, y, z, \mathcal{E})dr\right]d\mathcal{E}. \tag{4.6}$$

DEPTH-DEPENDENT MAGNIFICATION

Using equation (4.1), the simplified monoenergetic case, we can develop a more useful formulation which directly illustrates the "distortion" due to point-source geometry. The line integral element, dr, is decomposed as

$$dr = \sqrt{dx^2 + dy^2 + dz^2}. \tag{4.7}$$

The line integration, as seen in Fig. 4.2, takes place along a line defined as

$$x = \frac{x_d}{d}z \quad \text{and} \quad y = \frac{y_d}{d}z. \tag{4.8}$$

These equations allow us to rewrite the line integration of equation (4.1) in terms of the depth z using

$$dr = dz\sqrt{1 + \left(\frac{dx}{dz}\right)^2 + \left(\frac{dy}{dz}\right)^2}$$

$$\frac{dx}{dz} = \frac{x_d}{d} \quad \text{and} \quad \frac{dy}{dz} = \frac{y_d}{d}.$$

Substituting, we obtain

$$I_d(x_d, y_d) = I_i\exp\left[-\sqrt{1 + \frac{r_d^2}{d^2}}\int \mu_0\left(\frac{x_d}{d}z, \frac{y_d}{d}z, z\right)dz\right]. \tag{4.9}$$

The two-dimensional transmission function at any plane z is magnified by d/z in the detector plane, as can be seen in Fig. 4.2. We can therefore rewrite

the preceding equation as

$$I_d(x_d, y_d) = I_i \exp\left[-\sqrt{1 + \frac{r_d^2}{d^2}} \int_0^d \mu_0\left(\frac{x_d}{M(z)}, \frac{y_d}{M(z)}, z\right) dz\right] \tag{4.10}$$

where $M(z) = d/z$. This formulation can be arrived at through physical and geometric reasoning. The radical outside the integral is the obliquity factor due to the longer path lengths of rays through the object at greater angles to the normal. In certain geometries, as with relatively thin objects, it can be ignored.

EXAMPLES OF POINT-SOURCE GEOMETRY

As a first example, in Fig. 4.4 we study an infinite slab of thickness L which is centered at a depth of z_0 and has a uniform attenuation of μ_a. The three-dimensional attenuation coefficient can be expressed as

$$\mu_0(x, y, z) = \mu_a \operatorname{rect}\left(\frac{z - z_0}{L}\right). \tag{4.11}$$

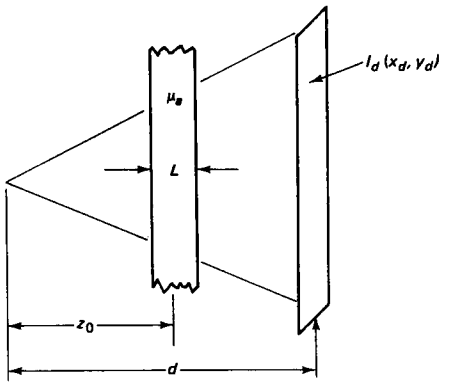

FIG. 4.4 Imaging of an infinite slab.

Since μ_0 is a function of z only, equation (4.10) simply involves the integral of a rect function, giving

$$I_d(x_d, y_d) = I_i \exp\left(-\sqrt{1 + \frac{r_d^2}{d^2}}\,\mu_a L\right). \tag{4.12}$$

For the case where $(r_d^2/d^2)\mu_a L \ll 1$, corresponding to a combination of a small attenuation coefficient, thin section, or regions close to the axis, the

detected output can be approximated by

$$I_d(x_d, y_d) \simeq I_i e^{-\mu_a L}.$$

Another interesting example of the effects of point-source geometry is the imaging of a rectangular object of unlimited extent in the x direction as shown in Fig. 4.5. The attenuation coefficient in space is defined by

$$\mu_0(x, y, z) = \mu_a \operatorname{rect}\left(\frac{y}{L}\right) \operatorname{rect}\left(\frac{z - z_0}{w}\right) \tag{4.13}$$

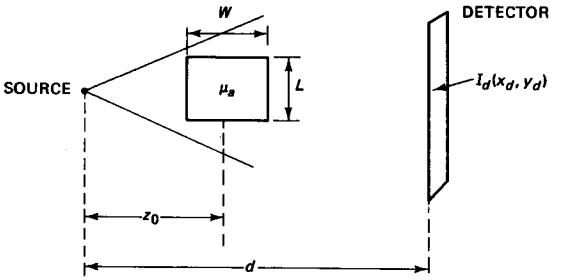

FIG. 4.5 Imaging of a rectangular object.

where μ_a is the uniform value of μ_0 throughout the object. The resultant intensity pattern at the detector becomes

$$I_d(x_d, y_d) = I_i \exp\left[-\sqrt{1 + \frac{r_d^2}{d^2}} \int \mu_a \operatorname{rect}\left(\frac{y_d z}{dL}\right) \operatorname{rect}\left(\frac{z - z_0}{w}\right) dz\right]. \tag{4.14}$$

The product of the two rect functions is used to define the upper and lower limits of integration corresponding to the overlap region of the two functions, as shown in Fig. 4.6.

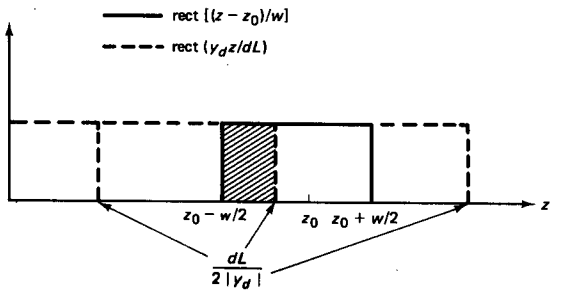

FIG. 4.6 Product of rect functions.

Rect $[(z - z_0)/w]$ is shown centered at z_0 with a width w. Three cases are shown for rect $y_d z/dL$, corresponding to three ranges of y_d. Since the function is symmetrical in y_d we can evaluate it for $|y_d|$, with the same image appearing at each side of the y_d axis. For values of $|y_d| > dL/(2z_0 - w)$, the rect functions do not overlap, providing an upper and lower limit of integration of $dL/2|y_d|$. Thus the integrated value is zero, corresponding to the lack of attenuation in the region where the rays miss the object. In the next region, for values of $|y_d|$ below $dL/(2z_0 - w)$ but above $dL/(2z_0 + w)$, the integration takes place in the shaded region from $z_0 - w/2$ to $dL/2|y_d|$, corresponding to rays cutting through the corners of the object. In the third region, where $|y_d| < dL/(2z_0 + w)$, the rays always go through the entire object. This corresponds to an integrated value of w since rect $(z - z_0)/w$ determines the limits of integration. The resultant equation is given by

$$I_d(x_d, y_d) = I_i \exp\left(-\mu_a \sqrt{1 + \frac{r_d^2}{d^2}} \int_{\min\left\{\frac{dL}{2|y_d|}\right\}}^{\min\left\{\frac{z_0 + w/2}{dL/2|y_d|}\right\}} dz\right). \tag{4.15}$$

Figure 4.7 illustrates the transmission I_d/I_i versus $|y_d|$, ignoring the obliquity factor $\sqrt{1 + r_d^2/d^2}$.

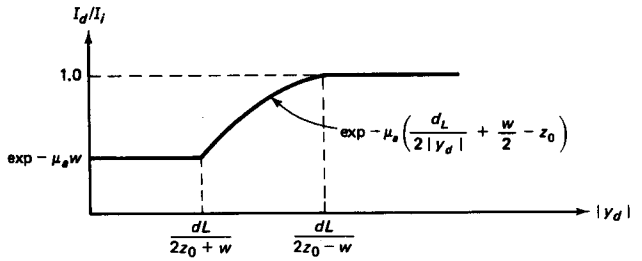

FIG. 4.7 Transmission of a rectangular object.

For very thin sections the attenuation coefficient can be characterized as

$$\mu_0(x, y, z) = \tau(x, y)\delta(z - z_0) \tag{4.16}$$

where $\tau(x, y)$ is the line integral of the attenuation coefficient at each point x, y. The resulting detected output is given by

$$I_d(x_d, y_d) = I_i \exp\left[-\sqrt{1 + \frac{r_d^2}{d^2}}\tau\left(\frac{x_d}{M}, \frac{y_d}{M}\right)\right] \tag{4.17}$$

where $M = d/z_0$. If we ignore the obliquity factor $\sqrt{1 + r_d^2/d^2}$, we can rewrite

the detected output as

$$I_d(x_d, y_d) = I_i t\left(\frac{x_d}{M}, \frac{y_d}{M}\right) \tag{4.18}$$

where the transmission function $t(x, y) = \exp[-\tau(x, y)]$.

In this form the geometric magnification factor of the diverging beam is evident where a plane at z_0 is magnified an amount d/z_0 in the detector plane. Planes close to the source receive a large magnification, while those close to the detector plane receive a magnification approaching unity.

The distortion of images due to point-source geometry can cause significant problems in clinical interpretation if the diagnostician does not take it into account [Christensen et al., 1978]. For example, in Fig. 4.8 the apparent relative

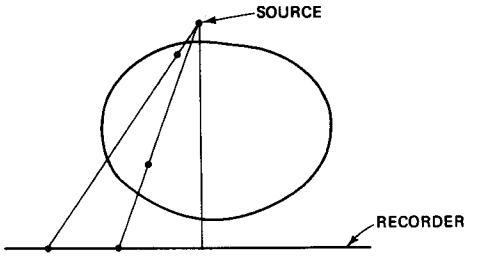

FIG. 4.8 Distortion of the relative position of two images with respect to the center lines.

radial position of two objects is distorted. Similarly, in Fig. 4.9, the apparent size of a tilted object depends on its position within the diverging beam. These examples are exaggerated compared to the usual clinical situation where the angular divergence of the beam is relatively small.

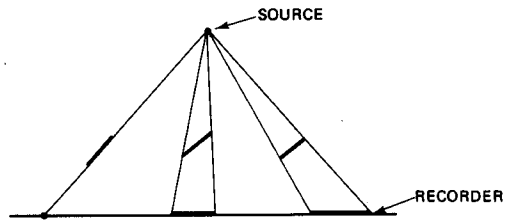

FIG. 4.9 Apparent size of a tilted object varies with its lateral position.

Figure 4.10 illustrates an x-ray photograph of an off-axis elongated plastic hollow cylinder. Note how the variation in magnification with depth gives the appearance of a truncated conical section, with one end experiencing greater magnification than the other.

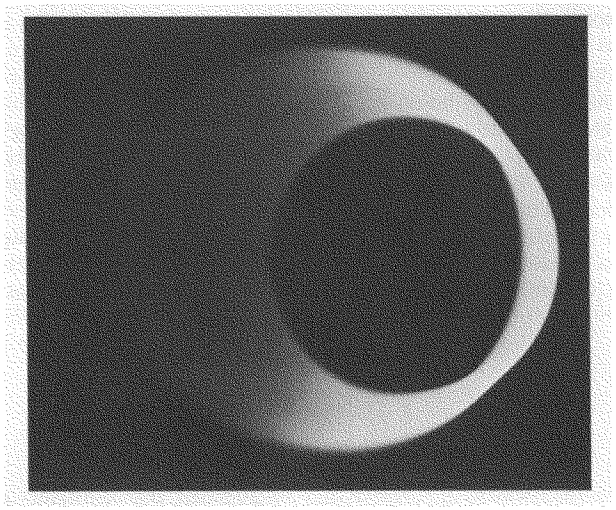

FIG. 4.10 X-ray photograph of a hollow plastic cylinder.

EXTENDED SOURCES

We have shown how the use of a point x-ray source produces images having a depth-dependent magnification which is a distortion when compared to the parallel geometry of Fig. 3.1. We now consider the effects of a finite source.

The x-ray source using a bombarded target, as in Fig. 4.1, has finite dimensions, which significantly affects the resolution of the detected image [Sprawls, 1977]. We first assume that the source is planar and parallel to the detector plane as shown in Fig. 4.11. If the object is an opaque plane at z having an array of pinholes, each pinhole will reproduce an inverted image of the source magnified by $(d - z)/z$, as indicated by the geometry. The point response $h(x_d, y_d)$ for a pinhole at the origin in plane z, for a source distribution $s(x_s, y_s)$, is of the form

$$h(x_d, y_d) = Ks\left(-x_d\frac{z}{d-z}, -y_d\frac{z}{d-z}\right) \tag{4.19}$$

$$= Ks\left(\frac{x_d}{m}, \frac{y_d}{m}\right) \tag{4.20}$$

where K is a proportionality constant and m, the magnification of the source due to a hole in plane z, is given by

$$m(z) = -\frac{d-z}{z} = 1 - M(z). \tag{4.21}$$

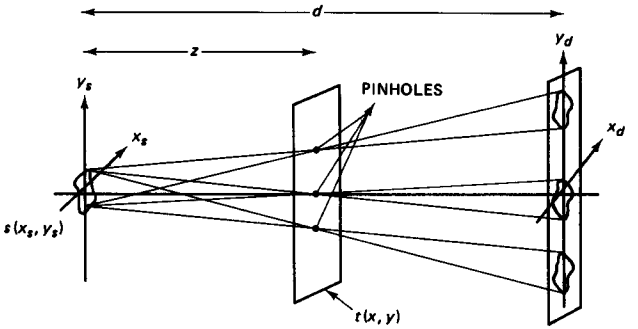

FIG. 4.11 Planar extended source.

Thus the magnification of the source image is 1 minus the magnification of the object. Since the response due to each pinhole is independent of its lateral position, the system is space invariant, as discussed in Chapter 2. The response to each isolated plane can be structured in convolution form and the spatial frequency domain can conveniently be used. The response to a transparency having transmission $t(x, y)$ in plane z is given by

$$I_d(x_d, y_d) = Kt\left(\frac{x_d}{M}, \frac{y_d}{M}\right) ** s\left(\frac{x_d}{m}, \frac{y_d}{m}\right). \tag{4.22}$$

This can be expressed in the Fourier domain as the product of the individual transforms, where

$$I_d(u, v) = KM^2m^2T(Mu, Mv)S(mu, mv) \tag{4.23}$$

where T and S are the Fourier transforms of t and s, and u and v are the spatial frequency coordinates.

ANALYSIS OF IMAGING USING PLANAR SOURCES

Having explored a simplified view of the effects of extended sources, we now formulate a more general analysis. Figure 4.12 illustrates an imaging system using a planar source $s(x_s, y_s)$. In our analysis, we first find the detected image due to a differential point at x_s, y_s on the source distribution. We then find the total detected intensity $I_d(x_d, y_d)$ by integrating over the entire source. The differential intensity at the detector plane in the absence of the object, $dI_i(x_d, y_d)$, due to a point at x_s, y_s is again given by

$$dI_i(x_d, y_d) = dI_0 \cos^3\theta$$

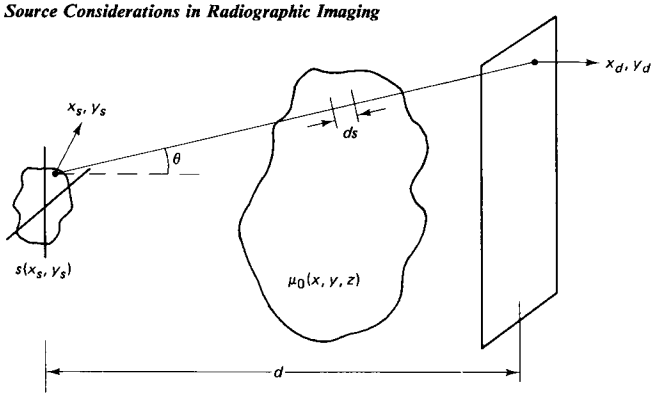

FIG. 4.12 Imaging, using a planar source.

as in (4.5). dI_0 is now defined as the differential detected intensity on the axis of the particular infinitesimal source point where $x_d = x_s$ and $y_d = y_s$, as given by

$$dI_0 = \frac{s(x_s, y_s)dx_s dy_s}{4\pi d^2}. \tag{4.24}$$

The angular distribution $\cos^3\theta$ is also measured from each infinitesimal source point as given by

$$\cos^3\theta = \left[1 + \left(\frac{x_d - x_s}{d}\right)^2 + \left(\frac{y_d - y_s}{d}\right)^2\right]^{-3/2}$$
$$= \frac{1}{(1 + r_{ds}^2/d^2)^{3/2}} \tag{4.25}$$

where $r_{ds} = [(x_d - x_s)^2 + (y_d - y_s)^2]^{1/2}$, the lateral distance between source and detector points.

Inserting the object with attenuation $\mu_0(x, y, z)$, the differential detected intensity due to each infinitesimal source point is given by

$$dI_d(x_d, y_d, x_s, y_s) = \frac{s(x_s, y_s)dx_s dy_s}{4\pi d^2(1 + r_{ds}^2/d^2)^{3/2}} \exp\left[-\int \mu_0(x, y, z)ds\right]$$
$$= dI_i \exp\left[-\int \mu_0(x, y, z)ds\right] \tag{4.26}$$

where ds is the element of line integration. Expanding ds, we obtain

$$ds = \sqrt{dx^2 + dy^2 + dz^2}$$
$$= dz\sqrt{1 + \left(\frac{dx}{dz}\right)^2 + \left(\frac{dy}{dz}\right)^2}. \tag{4.27}$$

Again parameterizing x and y coordinates in terms of z, the line integration

takes place along

$$x = \frac{x_d - x_s}{d}z + x_s \quad \text{and} \quad y = \frac{y_d - y_s}{d}z + y_s. \tag{4.28}$$

Substituting equations (4.27) and (4.28) into (4.26), we obtain

$$dI_d(x_d, y_d, x_s, y_s) = dI_i \exp\left[-\sqrt{1 + \frac{r_{ds}^2}{d^2}} \int \mu_0\left(\frac{x_d - x_s}{d}z + x_s, \frac{y_d - y_s}{d}z + y_s, z\right)dz\right]. \tag{4.29}$$

Using the previously defined object magnification $M = d/z$ and source magnification $m = -(d - z)/z$, (4.29) becomes

$$dI_d(x_d, y_d, x_s, y_s) = dI_i \exp\left[-\sqrt{1 + \frac{r_{ds}^2}{d^2}} \int \mu_0\left(\frac{x_d - mx_s}{M}, \frac{y_d - my_s}{M}, z\right)dz\right]. \tag{4.30}$$

The detected image due to the entire source, $I_d(x_d, y_d)$, is obtained by integrating the image due to a source point $dI_d(x_d, y_d, x_s, y_s)$ over the entire source as given by

$$I_d(x_d, y_d) = \iint dI_d(x_d, y_d, x_s, , y_s)$$
$$= \frac{1}{4\pi d^2}\iint \frac{s(x_s, y_s)}{(1 + r_{ds}^2/d^2)^{3/2}} \exp\left[-\sqrt{1 + \frac{r_{ds}^2}{d^2}} \int \mu_0\left(\frac{x_d - mx_s}{M}, \frac{y_d - my_s}{M}, z\right)dz\right]dx_s dy_s. \tag{4.31}$$

For the more complete polyenergetic case, both s and μ are functions of energy and the entire expression is integrated over the energy spectrum.

We can simplify equation (4.31) to provide more insight into the imaging process. We first assume that r_{ds} is sufficiently smaller than d so that we can ignore the two obliquity factors relating to the falloff in source intensity and the increased path through the object. We study a thin object at $z = z_0$ again characterized by

$$\mu_0(x, y, z) = \tau(x, y)\delta(z - z_0). \tag{4.32}$$

The resultant detected image intensity becomes

$$I_d(x_d, y_d) = \frac{1}{4\pi d^2}\iint s(x_s, y_s) \exp\left[-\tau\left(\frac{x_d - mx_s}{M}, \frac{y_d - my_s}{M}\right)\right]dx_s dy_s. \tag{4.33}$$

To place this expression in the desired space-invariant convolutional form, we use the substitution

$$x' = mx_s, \quad y' = my_s \tag{4.34}$$

to provide

$$I_d(x_d, y_d) = \frac{1}{4\pi d^2 m^2} s\left(\frac{x_d}{m}, \frac{y_d}{m}\right) ** \exp\left[-\tau\left(\frac{x_d}{M}, \frac{y_d}{M}\right)\right]. \tag{4.35}$$

Using the previously defined $t(x, y) = \exp[-\tau(x, y)]$, we obtain the simplified convolution expression

$$I_d(x_d, y_d) = \frac{1}{4\pi d^2 m^2} s\left(\frac{x_d}{m}, \frac{y_d}{m}\right) ** t\left(\frac{x_d}{M}, \frac{y_d}{M}\right) \tag{4.36}$$

which is identical to (4.22). This result was derived using a superposition of source points each separately imaging the object. This provided a general result, equation (4.31), for imaging any object. An alternative, simpler approach, however, can be used for the case of a planar object with the obliquity factors ignored, giving the same result as in equation (4.36).

ALTERNATIVE ANALYSIS USING PLANAR OBJECTS

In this approach we find the detected intensity from the entire source due to a transparency consisting of an impulse where $t(x, y) = \delta(x - x', y - y')$, as shown in Fig. 4.13. The resultant intensity at the detector plane or impulse response $h(x_d, y_d, x', y')$ is given by

$$h(x_d, y_d, x', y') = \frac{\eta}{m^2} s\left(\frac{x_d - Mx'}{m}, \frac{y_d - My'}{m}\right) \tag{4.37}$$

where η is the collection efficiency of the pinhole as given by

$$\eta = \frac{\Omega}{4\pi} \tag{4.38}$$

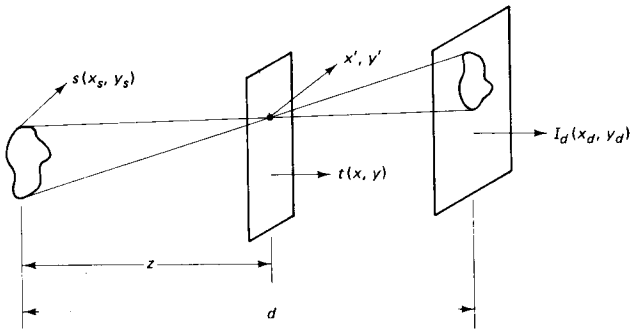

FIG. 4.13 Impulse response with an extended source.

where Ω is the solid collection angle of the pinhole. Equation (4.37) is derived by direct geometric projection with a magnification m and a translation weighted by M. The term η/m^2 is the collection efficiency divided by the ratio of image and source areas. Ignoring obliquity is equivalent to assuming that the solid angle of the unity area pinhole is $1/z^2$ over the entire transparency. With this approximation, the detected intensity is given by

$$I(x_d, y_d) = \iint h(x_d, y_d, x', y')t(x', y')dx'dy'$$

$$= \frac{1}{4\pi z^2 m^2} \iint t(x', y')s\left(\frac{x_d - Mx'}{m}, \frac{y_d - My'}{m}\right)dx'dy'. \tag{4.39}$$

Substituting $x'' = Mx'$ and $y'' = My'$ provides a convolution relationship given by

$$I_d(x_d, y_d) = \frac{1}{4\pi z^2 m^2 M^2} t\left(\frac{x_d}{M}, \frac{y_d}{M}\right) ** s\left(\frac{x_d}{m}, \frac{y_d}{m}\right) \tag{4.40}$$

which is identical to the previously derived equation (4.36).

Effects of Source Size

Equation (4.40) illustrates the basic problem of the loss of resolution due to source size. For object planes close to the detector where $M \simeq 1$ and $m \simeq 0$, the image has unity magnification and is not blurred by the source, no matter what its size, since $(1/m^2)s(x/m, y/m)$ approaches a delta function. For object planes closer to the source, for example at $z = d/2$ where $M = 2$ and $|m| = 1$, the object plane will be blurred by the source size itself. Attempts at greater magnifications will have greater blurring since $|m| = M - 1$. Figure 4.14 illustrates two x-ray photographs of a high-resolution test object taken with different magnifications. In the case of unity magnification the array of holes are well resolved due to the lack of blur from the source function. With a magnification of 2, however, the smaller holes are clearly blurred by the source function.

SIMPLIFYING RELATIONSHIPS USING SOLID OBJECTS

The simplified convolution relationships (4.36) and (4.40) were derived for a planar object with the only approximations being the neglecting of obliquity factors. However, for the solid object, even with the neglecting of obliquity, the nonlinear relationship prevents us from forming a convolution relationship.

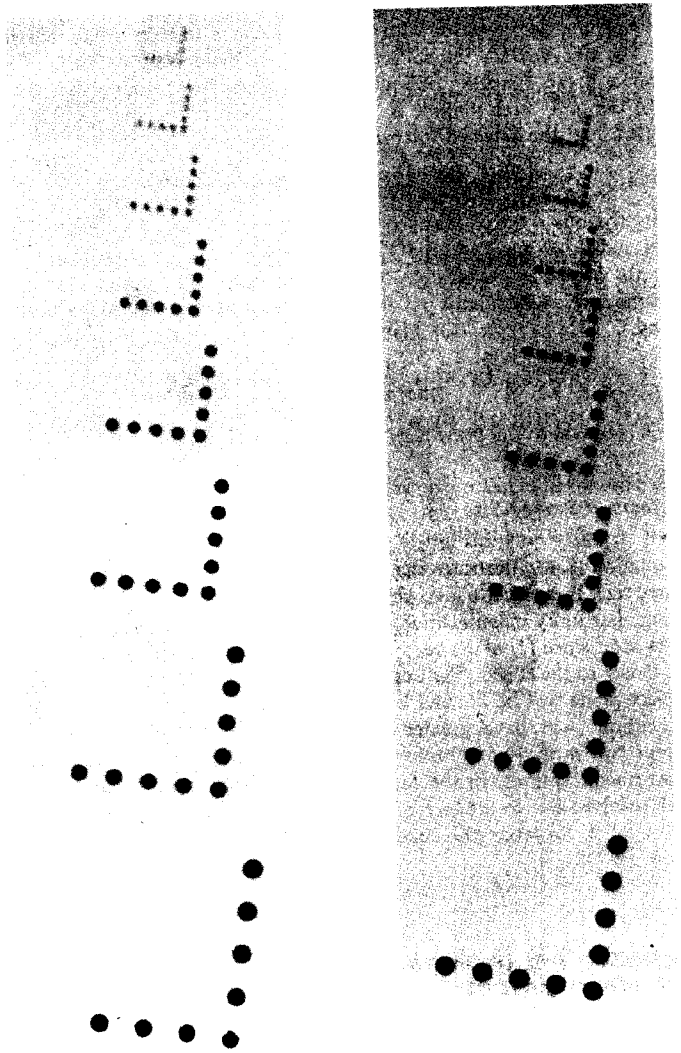

FIG. 4.14 X-ray images of a planar object, using different magnifications.

Repeating (4.31) without the obliquity factors, we have

$$I_d(x_d, y_d) = \frac{1}{4\pi d^2} \int\int s(x_s, y_s) \exp\left[-\int \mu_0\left(\frac{x_d - mx_s}{M}, \frac{y_d - my_s}{M}, z\right)dz\right]dx_s dy_s. \tag{4.41}$$

In general the three-dimensional attenuation coefficient of the object $\mu(x, y, z)$ must be used to solve for the intensity. Unfortunately, this relationship does not provide the insightful convolution relationship which serves to directly indicate the system performance and facilitate the use of frequency analysis.

Using various approximations, each having different degrees of validity, equation (4.41) can be linearized to provide a convolution form. One approach is the modeling of the solid object as an array of planar objects as given by

$$\mu_0(x, y, z) = \sum_i \tau_i(x, y)\delta(z - z_i) \tag{4.42}$$

with the resultant detected intensity

$$I_d(x_d, y_d) = \frac{1}{4\pi d^2} \int\int s(x_s, y_s) \exp\left\{-\sum_i\left[\tau_i\left(\frac{x_d - m_i x_s}{M_i}, \frac{y_d - m_i y_s}{M_i}\right)\right]\right\} dx_s dy_s \tag{4.43}$$

where $m_i = -(d - z_i)/z_i$ and $M_i = d/z_i$. If we make the assumption $\int \mu dz < 1$, namely that the attenuation through any path is relatively small, we can linearize the exponential where $\exp(-\int \mu dz) \simeq 1 - \int \mu dz$, giving

$$I_d(x_d, y_d) \simeq I_i - \sum_i \frac{1}{4\pi d^2 m_i^2} s\left(\frac{x_d}{m_i}, \frac{y_d}{m_i}\right) ** \tau_i\left(\frac{x_d}{M_i}, \frac{y_d}{M_i}\right) \tag{4.44}$$

where $I_i = (1/4\pi d^2) \int\int s(x_s, y_s)dx_s dy_s$, the intensity in the absence of an object.

This formulation (4.44) provides a convolution relationship for all planes of a solid object. Unfortunately, the approximation used in the derivation, $\int \mu dz < 1$, is quite inaccurate except for very thin portions of the body. At diagnostic energy levels the attenuation coefficient of most soft tissue is about $0.2\ \text{cm}^{-1}$. Thus a typical 20-cm depth provides $\int \mu dz \simeq 4$, which makes the approximation unreasonable.

An alternative approach is to assume that most body tissue has an attenuation coefficient similar to that of water, so that the attenuation coefficient is decomposed as

$$\mu_0(x, y, z) = \mu_w(x, y, z) + \mu_\Delta(x, y, z) \tag{4.45}$$

where μ_w is the attenuation coefficient of water and μ_Δ is the departure from that of water. We can now more legitimately assume that $\int \mu_\Delta dz < 1$. Those coefficients that do depart significantly from water, namely air and bone, are often associated with relatively short path lengths, so that the assumption can remain valid. Substituting (4.45) in (4.41) and using the assumption above,

we obtain

$$I_d(x_d, y_d) \simeq \frac{1}{4\pi d^2} \iint s(x_s, y_s) \exp\left[-\int \mu_w\left(\frac{x_d - mx_s}{M}, \frac{y_d - my_s}{M}, z\right)dz\right] \times \left[1 - \int \mu_\Delta\left(\frac{x_d - mx_s}{M}, \frac{y_d - my_s}{M}, z\right)dz\right]dx_s dy_s. \quad (4.46)$$

The first exponential in the integral represents the line integral of the object consisting of uniform tissue having attenuation coefficient μ_w. Because of the uniformity we can make the approximation

$$\mu_w\left(\frac{x_d - mx_s}{M}, \frac{y_d - my_s}{M}, z\right) \simeq \mu_w\left(\frac{x_d}{M}, \frac{y_d}{M}, z\right). \quad (4.47)$$

This approximation is valid within the interior of the object. It fails, however, at the boundaries of the object, where the attenuation coefficient goes abruptly from μ_w to zero. Using this approximation, and restructuring the integration involving μ_Δ as a summation of planes, as in (4.42) to (4.44), we obtain

$$I_d(x_d, y_d) \simeq T_w\left[I_l - \sum_i \frac{1}{4\pi d^2 m_i^2} s\left(\frac{x_d}{m_i}, \frac{y_d}{m_i}\right) ** \tau_{\Delta i}\left(\frac{x_d}{M_i}, \frac{y_d}{M_i}\right)\right] \quad (4.48)$$

where

$$T_w = \exp\left[-\int \mu_w\left(\frac{x_d}{M}, \frac{y_d}{M}, z\right)dz\right].$$

Equation (4.48) provides a convolution relationship with each plane using more valid approximations than that of (4.44). T_w represents the transmission through the object as if it were composed uniformly of water and the source was a point. It should be emphasized that, although equation (4.48) provides a reasonable basis for calculating the intensity due to a solid object, that is not the main reason for its presentation. The principal conclusion to be drawn from this development is that it is reasonable to study the response to an individual plane within a volume using the simplified convolutional relationship of equation (4.36).

Although (4.44) and (4.48) provide the elegance of the convolution relationship, for the general three-dimensional object, (4.31) or (4.41) must be used. For example, using the rectangular object of Fig. 4.5 with equation (4.41), we obtain

$$I_d(x_d, y_d) = \frac{1}{4\pi d^2} \iint s(x_s, y_s) \exp\left[-\mu_a \int \text{rect}\left(\frac{y_d - my_s}{ML}\right) \text{rect}\left(\frac{z - z_0}{w}\right)dz\right] \times dx_s dy_s. \quad (4.49)$$

In this case the limits of integration are no longer symmetrical in y_d. The integral over the object is given by

$$\int \text{rect}\left(\frac{y_d - my_s}{ML}\right) \text{rect}\left(\frac{z - z_0}{w}\right)dz = \int_{\min\left\{\max\left\{\frac{-dL/2 - y_s d}{y_d - y_s}, \frac{dL/2 - y_s d}{y_d - y_s}\right\}\right.}^{\min\left\{\max\left\{\frac{-dL/2 - y_s d}{y_d - y_s}, \frac{dL/2 - y_s d}{y_d - y_s}\right\}\right.} dz. \quad (4.50)$$

These limits define five zones of integration corresponding to the regions delineated by the intersection of the rays from the finite source with the four corners of the rectangle.

In general, in the study of radiographic imaging, the simplified convolutional relationships of a single plane are preferred since they provide profound insight into the performance-limiting factors. To review the development of the convolutional approach, we first showed that, for a planar object, if the relatively small obliquity factors are neglected, the resultant image is the convolution of the magnified transparency with a magnified source. For the solid object, we first modeled it as an array of planes and showed that the convolutional form would again apply if the total line integral of the attenuation coefficient is quite small so that the exponential could be linearized. Since this is not the usual case, we then modeled the solid object as a sum of a water coefficient, its dominant component, and a difference from this coefficient. Since the line integral of the difference component is quite small, we could linearize this portion of the expression and express each plane in convolutional form. As indicated, the motivation for this exercise was not primarily to establish an analytic procedure to deal with solid objects. It was, rather, a justification for analyzing systems by their response to a single planar object. We have shown that the simplified planar object analysis does indeed predict the performance of complex *volumetric* objects.

NONPARALLEL SOURCE DISTRIBUTIONS

In most x-ray tubes, as shown in Fig. 4.1, the source is not parallel to the plane of the detector. This results in a different point-spread function for each region of the detector plane. In general the source is a three-dimensional surface $s(x_s, y_s, z_s)$. Using the same type of derivation as that of the planar source, the generalized expression for the recorded intensity becomes

$$I_d(x_d, y_d) = \frac{1}{4\pi d^2} \iiint \frac{s(x_s, y_s, z_s)}{\left[1 + \left(\frac{r_{ds}}{d - z_s}\right)^2\right]^{3/2}} \exp\left[-\sqrt{1 + \left(\frac{r_{ds}}{d - z_s}\right)^2} \times \int \mu_0\left(\frac{x_d - m'x_s}{M'}, \frac{y_d - m'y_s}{M'}, z\right)dz\right]dx_s dy_s dz_s \quad (4.51)$$

where

$$m' = -\frac{d - z}{z - z_s} \quad \text{and} \quad M' = \frac{d - z_s}{z - z_s}.$$

As shown with the rotating anode tube of Fig. 4.1, the conventional x-ray tube has a source that can be approximated as a planar surface which is tilted with respect to the detector. The effects of this source distribution are illustrated in

Fig. 4.15. As can be seen, the projected source size varies significantly for different y positions on the planar object $t(x, y)$. The source geometry is modeled by setting $z_s \quad \alpha y_s$, where α is the tangent of the angle between the source plane and the vertical.

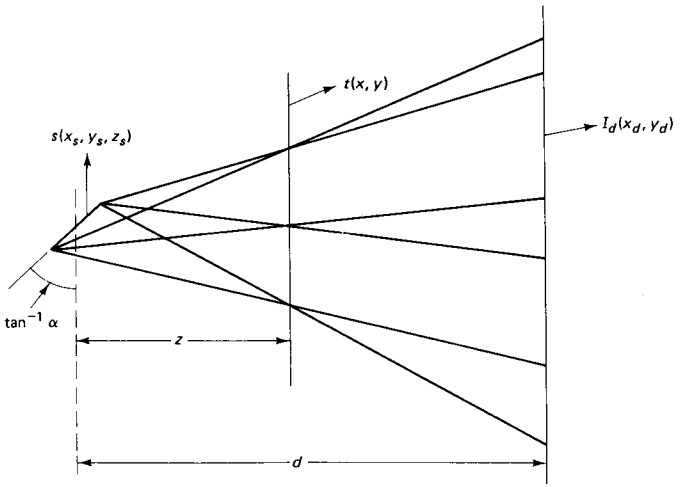

FIG. 4.15 Point response variations due to a tilted source.

For the tilted source case we can again evaluate the impulse response using a pinhole at x', y' as in Fig. 4.13. Since, in general, the magnifications will be different along each axis, we can rewrite equation (4.37) as

$$h(x_d, y_d, x', y') = \frac{\eta}{m_x m_y} s\left(\frac{x_d - M_x x'}{m_x}, \frac{y_d - M_y y'}{m_y}\right) \tag{4.52}$$

where m_x, m_y, M_x, and M_y are the incremental magnifications as given by

$$\begin{aligned} m_x &= \frac{\partial x_d}{\partial x_s} \quad \text{and} \quad m_y = \frac{\partial y_d}{\partial y_s} \\ M_x &= \frac{\partial x_d}{\partial x'} \quad \text{and} \quad M_y = \frac{\partial y_d}{\partial y'}. \end{aligned} \tag{4.53}$$

In the case of the planar source parallel to the detector, these magnifications were constants independent of source and object coordinates. For the tilted source these constants are evaluated with the aid of Fig. 4.16. The values of m' and M' for the tilted source, by geometry, become

$$m' = -\frac{d - z}{z - \alpha y_s} \quad \text{and} \quad M' = \frac{d - \alpha y_s}{z - \alpha y_s}. \tag{4.54}$$

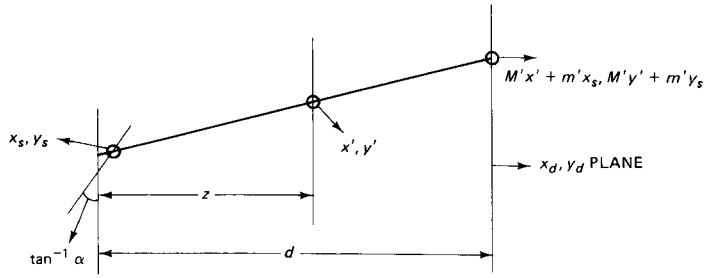

FIG. 4.16 Ray tracing for a tilted source.

The incremental magnifications are found by appropriately differentiating the recorder coordinates in Fig. 4.16, where $x_d = M'x' + m'x_s$ and $y_d = M'y' + m'y_s$. These are given by

$$m_x = m' = -\frac{d - z}{z - \alpha y_s}, \quad m_y = -\frac{(d - z)(z - \alpha y')}{(z - \alpha y_s)^2},$$
$$\text{and} \quad M_x = M_y = \frac{d - \alpha y_s}{z - \alpha y_s}. \tag{4.55}$$

For any sources of interest the source size will be significantly smaller than the object depth z. Thus $z \gg \alpha y_s$ and $d \gg \alpha y_s$. We then get the approximate relationships

$$m_x \simeq -\frac{d - z}{z} = m, \quad m_y \simeq -\frac{(d - z)(z - \alpha y')}{z^2} = m\left(\frac{1 - \alpha y'}{z}\right),$$
$$\text{and} \quad M_x = M_y \simeq \frac{d}{z} = M. \tag{4.56}$$

Using these relationships the point response, ignoring obliquity, is given by

$$h(x_d, y_d, x', y') = \frac{1}{4\pi z^2 m^2 (1 - \alpha y'/z)} s\left[\frac{x_d - Mx'}{m}, \frac{y_d - My'}{m(1 - \alpha y'/z)}\right]. \tag{4.57}$$

This impulse response confirms the behavior shown in Fig. 4.15, where the y magnification changes significantly with the vertical position of the object point y'. The x magnification remains essentially unchanged. For the case of an impulse at $y' = z/\alpha$, the detector sees the edge of the source, resulting in a line image. Equation (4.57) then reduces to a delta function in the y dimension.

For the intensity due to a general transparency $t(x, y)$, we use the impulse response in the superposition integral. Making the substitutions $x'' = Mx'$ and $y'' = My'$, the detected intensity becomes

$$I_d(x_d, y_d) = \frac{1}{4\pi d^2 m^2} \int\int \frac{1}{1 - \alpha y''/Mz} s\left(\frac{x_d - x''}{m}, \frac{y_d - y''}{m(1 - \alpha y''/Mz)}\right) \times t\left(\frac{x''}{M}, \frac{y''}{M}\right) dx'' dy''. \tag{4.58}$$

Despite the appropriate substitutions, equation (4.58) remains space variant because of the variation in the y magnification with the object coordinate. In an attempt to use the convolution formulation, we can divide the object plane into narrow horizontal strips at each value of y'. These strips form space-invariant or isoplanatic patches within which the impulse response is constant. Each horizontal strip at an object coordinate y' corresponds to a horizontal strip at the detector plane at coordinate $y_d = My'$. An approximate convolutional relationship can be structured at each horizontal strip by reformulating equation (4.58) as

$$I_d(x_d, y_d, y'_d) \simeq \frac{1}{4\pi d^2 m^2 (1 - \alpha y'_d/d)} s\left(\frac{x_d}{m}, \frac{y_d}{m(1 - \alpha y'_d/d)}\right) ** t\left(\frac{x_d}{M}, \frac{y_d}{M}\right) \tag{4.59}$$

where y'_d is the detector coordinate of the region of interest and is a constant in the convolution operation. The variation of vertical resolution with y'_d is clearly indicated. This relationship can be transformed into the frequency domain as

$$I_d(u, v, y'_d) = \frac{M^2}{4\pi d^2} S\left[mu, m\left(1 - \frac{\alpha y'_d}{d}\right)v\right] T(Mu, Mv). \tag{4.60}$$

Again at $y' = z/\alpha$ corresponding to $y'_d = d/\alpha$, we see the infinite bandwidth in the v dimension.

We have shown that the commonly used rotating anode tube can be structured as a tilted planar source. Although all the magnifications become a function of object position, the only one that changes significantly is the source magnification in the direction of the tilt. Using formulations for the incremental magnifications, with appropriate approximations, we develop an impulse response which is a function of the object position in the direction of the tilt. This allows an approximate convolution relationship which serves to illustrate the nature of the blur function.

EFFECTS OF OBJECT MOTION

The oversimplified solution to the problem of a finite source size is to use an extremely small source. These sources, however, have reduced power output, requiring longer exposure intervals, resulting in blurring due to the motion of the object under study. These motions are either those of uncooperative patients, such as children, or the physiological body motions of the respiratory, cardiovascular, and gastrointestinal systems.

The blurring effect of motion can be considered as a linear system parameter similar to that of the source size. Using the basic system of Fig. 4.13, consider the pinhole aperture moving uniformly in the x direction with a velocity v during the exposure interval T. The image movement at the recorder plane, by

geometry, is MvT. The resultant recorded intensity is given by

$$I_d(x_d, y_d) = \frac{1}{4\pi d^2 m^2} t\left(\frac{x_d}{M}, \frac{y_d}{M}\right) ** s\left(\frac{x_d}{m}, \frac{y_d}{m}\right) * \frac{1}{MvT} \operatorname{rect}\left(\frac{x_d}{MvT}\right). \tag{4.61}$$

Thus the motion blurring is minimized by a short exposure time T.

Equation (4.61) can be restructured to emphasize the trade-off between source size and exposure time as limiting the system resolution. The energy density of the source $s(x, y)$ can be written as the product of a power density $p(x, y)$ and the exposure time T. The total source energy E_s is thus given by $T \iint p(x, y)dxdy$. To minimize the exposure time, for a given source energy, the source is operated at its maximum power density $P_{\max}$, usually determined by the temperature limit. If we assume that the source is emitting uniformly and has an extent of $a(x, y)$, equation (4.61) becomes

$$I_d(x_d, y_d) = \frac{t(x_d/M, y_d/M)}{4\pi d^2 m^2} ** P_{\max} T a\left(\frac{x_d}{m}, \frac{y_d}{m}\right) * \frac{P_{\max} \iint a(x, y)dxdy}{MvE_s} \times \operatorname{rect}\left[\frac{x_d P_{\max} \iint a(x, y)dxdy}{MvE_s}\right] \tag{4.62}$$

where $a(x, y)$ is a binary function defining the extent of the uniform source. The T in the rect function due to motion has been replaced by the source energy divided by the integrated source power. For a square source where $a(x, y) = \operatorname{rect} x/L \operatorname{rect} y/L$, the impulse response is given by

$$h(x_d, y_d) = K \operatorname{rect}\left(\frac{x_d}{mL}, \frac{y_d}{mL}\right) * \operatorname{rect}\left(\frac{x_d}{MvE_s/P_{\max}L^2}\right). \tag{4.63}$$

As indicated in (4.63), a larger source size results in a decreased motion blurring, and vice versa. The total extent of the point response in the x direction, X, due to source size and motion, is given by

$$X = |m|L + \frac{MvE_s}{P_{\max}L^2}. \tag{4.64}$$

This expression can be minimized with respect to L, giving

$$L_{\min} = \left(\frac{2MvE_s}{P_{\max}|m|}\right)^{1/3}. \tag{4.65}$$

A square source size having this dimension will provide the smallest point response in the x direction. The corresponding exposure time T is given by

$$T = \frac{E_s}{P_{\max}L_{\min}^2} = \left(\frac{E_s}{P_{\max}}\right)^{1/3} \left(\frac{|m|}{2Mv}\right)^{2/3}. \tag{4.66}$$

Thus, as the velocity of the object increases, the optimum source size becomes larger and the exposure time correspondingly smaller.

REPRESENTATIVE SOURCE CONFIGURATIONS

Standard x-ray tubes use directly heated cathodes consisting of a coiled filament within a focusing cup. The resultant electron optics often results in two distinct areas on the rotating anode which are being bombarded with electrons and producing x-rays, as illustrated in Fig. 4.17. The source function can be approximated as two narrow rectangles each $w \times L$ separated by W, as given by

$$s(x, y) = \left[\text{rect}\left(\frac{x - W/2}{w}\right) + \text{rect}\left(\frac{x + W/2}{w}\right)\right]\text{rect}\left(\frac{y}{L}\right). \tag{4.67}$$

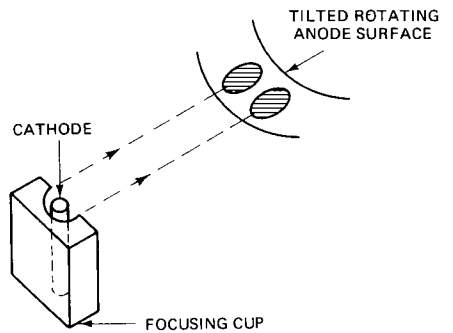

FIG. 4.17 Typical focal spot shape in x-ray tubes.

Typical dimensions for W and L vary from 0.3 to 2.5 mm. This represents a relatively poor response in the x direction, which can distort vertical edges. One indication of the problem is the Fourier transform of the source distribution, as given by

$$S(u, v) = 2wL \cos(\pi W u)\,\text{sinc}(wu)\,\text{sinc}(Lv). \tag{4.68}$$

The cosine function makes the response highly oscillatory in the x direction. Of course, as previously indicated, the system response to a source function is determined by the source magnification m. Thus object planes close to the detector, where m is relatively small, will be relatively independent of the source size and shape.

Many efforts are under way to provide source configurations which are both smaller and have preferred shapes. In some x-ray tubes additional focusing fields are applied to cause the electron beam to produce a more desirable single spot. Microfocus tubes are available which use electron guns and produce focal spots of 50 to 200 microns. Field emission tubes have no heated filament and emit electrons from sharp points on a cylindrical cathode where the electric

field is very high. These electrons impinge on a conical anode within the cylinder, resulting in a relatively large annular source size. These tubes use relatively high voltages and low currents and have not achieved widespread use.

Focal spots are generally measured using a pinhole camera. A small hole is placed in a relatively opaque sheet of high-atomic-number metal such as lead or gold. The pinhole is placed between the source and the film recorder. Ignoring obliquity factors, the resultant source image is given by

$$I_d(x_d, y_d) = \frac{1}{4\pi z^2 m^2 M^2} p\left(\frac{x_d}{M}, \frac{y_d}{M}\right) ** s\left(\frac{x_d}{m}, \frac{y_d}{m}\right) \tag{4.69}$$

where $p(x, y)$ represents the pinhole. The detected image will essentially represent the source as long as the magnified pinhole $p(x/M, y/M)$ is appreciably smaller in extent than the magnified source image $s(x/m, y/m)$. In this way the pinhole acts as a two-dimensional delta function, reproducing the source image. Typically, the pinhole is midway between source and detector with $|m| \simeq 1$ and $M \simeq 2$, so that the source image is approximately actual size. A relatively high resolution recorder, consisting of film only, is used to preserve the source image.

PROBLEMS

4.1 (a) Using a point-source x-ray system a distance d from the detector, find an approximate expression for the distance from the center of the detector r_d where the incident intensity has fallen off a fractional amount Δ, where $\Delta \ll 1$.

(b) Using the same system, a slab of material of thickness W and attenuation coefficient μ_0, parallel to the detector, is placed in the x-ray path. Neglecting the falloff in incident intensity, calculate the value of r_d at which the detected intensity has fallen off a fractional amount Δ, where $\Delta \ll 1$.

(c) For parts (a) and (b), calculate r_d for $d = 1$ meter, $W = 20$ cm, $\mu_0 = 0.25\ \text{cm}^{-1}$, and $\Delta = 1\%$.

4.2 As shown in Fig. P4.2, a cylindrical bone of infinite length is embedded in a layer of soft tissue of infinite extent. The linear attenuation coefficient of the bone is μ_b and that of the soft tissue is μ_w. The incident intensity is I_0 using parallel x-rays.

(a) Find an expression for I_d, the detected intensity.

(b) What is the ratio of the detected intensity through the maximum bone thickness at y_d 0 to that of the soft-tissue-only region where $y_d > R$?

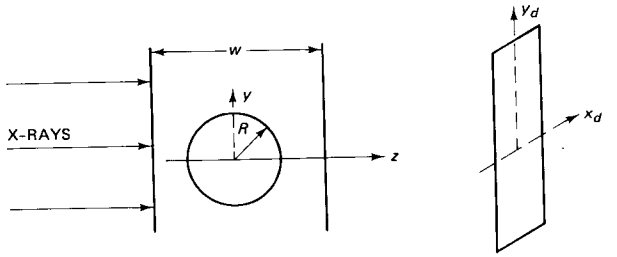

FIG. P4.2

(c) Calculate this ratio for $W = 20$ cm, $R = 0.5$ cm, using the curves of Fig. 3.7, where the soft tissue is muscle having a density of 1.0 and the bone density is 1.75. Perform the calculation for x-ray photon energies of 30 and 100 kev.

4.3 A cylindrical object having an attenuation coefficient μ_0 is positioned in a point-source x-ray system as shown in Fig. P4.3.

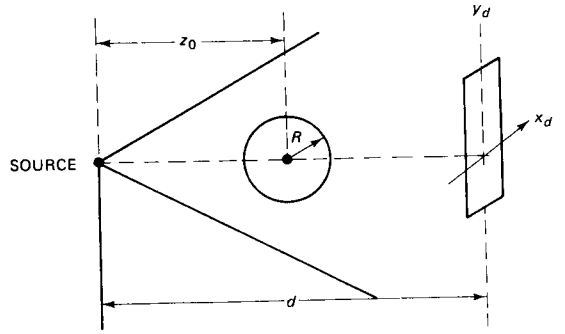

FIG. P4.3

(a) Find an expression for I_d, neglecting the falloff of the source intensity over the detector plane due to obliquity.

(b) Find an expression for I_d using the object in Problem 4.2 with the cylinder in a layer of soft tissue.

4.4 A cylinder of attenuation coefficient μ, radius R, and length L is placed on the axis of an x-ray imaging system as shown in Fig. P4.4. Neglecting all obliquity factors, find an expression for I_d versus r_d, where the intensity in the absence of the object is a uniform I_0.

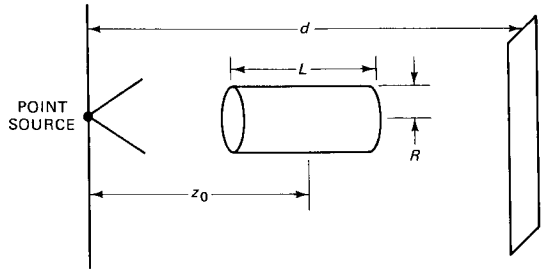

FIG. P4.4

4.5 A rectangular x-ray source, $s(x_s, y_s) = \text{rect}\,(x/X)\ \text{rect}\,(y/Y)$, is used with two opaque, semi-infinite planes as shown in Fig. P4.5. Ignoring all obliquity factors, plot the intensity versus y_d on the detector plane labeling all break points.

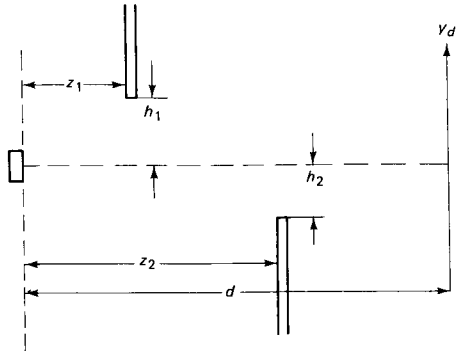

FIG. P4.5

4.6 An $L \times L$ x-ray source, having unity intensity, parallel to and a distance d from the recorder, is used to image a planar transparency a distance z from the source having a transmission

$$t = \tfrac{1}{2} + \tfrac{1}{2}\cos 2\pi a y$$

(a) Ignoring obliquity, find an expression for the intensity at the recorder plane. (Do not leave in convolutional form.)

(b) Repeat part (a) where the source is tilted at angle $\tan^{-1}\alpha$, where $\alpha = z_s/y_s$, and the projected size of the source in the xy plane continues to be $L \times L$.

4.7 A tilted source is used to image an opaque planar tilted object infinite in extent and containing three pinholes of equal size as shown in Fig. P4.7. Neglecting obliquity, plot I_d versus y_d, indicating the relative amplitudes and the position of the break points. Space invariance can be assumed in the vicinity of the pinhole images.

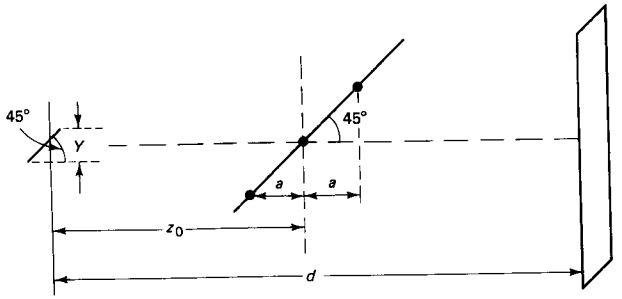

FIG. P4.7

4.8 A rectangular source tilted by an angle θ is used to image an opaque object tilted at 45° as shown in Fig. P4.8. The projection of the source Y is significantly smaller than all other dimensions. Neglecting obliquity factors, plot the relative detected intensity in the y_d direction labeling the y_d axis at the break points. [*Hint*: Assume space invariance in the vicinity of the break points.]

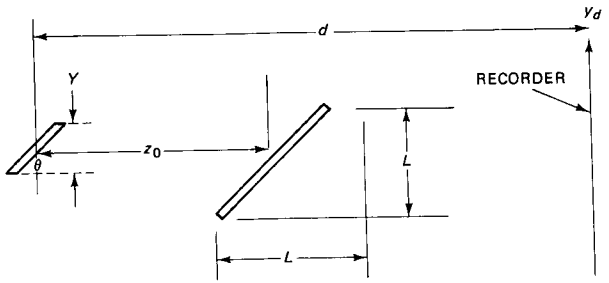

FIG. P4.8

4.9 A source tilted at an angle of 45° has a projected intensity $s(x, y) = K$ circ (r/r_0). It is used to image a transparency at $z = z_0$, having a transmission $t(x, y) = \sum_i \delta(x)\delta(y - i)$. Find the resultant intensity at $z = d$, neglecting obliquity.

5

Recorder Resolution Considerations

We have thus far considered resolution limitations due to the x-ray source. The other important resolution-limiting factor in the system is the x-ray recorder, where the image itself is formed. The principal difficulty is in the attaining of the desired high resolution while maintaining a relatively high quantum or capture efficiency. The quantum or capture efficiency represents the fraction of photons that interact within the recorder material. As will be shown in Chapter 6, the number of captured photons per picture element governs the resultant signal-to-noise ratio. This SNR will be shown to be given by

$$\text{SNR} = C\sqrt{\eta N} \tag{5.1}$$

where N is the number of photons per picture element impinging on the recorder, η is the quantum or capture efficiency, and C is the contrast of the structure of interest. A thick recorder has a high quantum efficiency but, as will be shown, exhibits poor resolution. Similarly, very thin recorders exhibit negligible blurring due to spreading, but capture relatively few of the photons.